

# Application of Exactly Linearized Error Transport Equations to AIAA CFD Prediction Workshops

Joseph M. Derlaga\* and Michael A. Park†

*NASA Langley Research Center, Hampton, Virginia, 23681*

Sriram K. Rallabhandi‡

*National Institute of Aerospace, Hampton, Virginia, 23666*

The computational fluid dynamics (CFD) prediction workshops sponsored by the AIAA have created invaluable opportunities in which to discuss the predictive capabilities of CFD in areas in which it has struggled, e.g., cruise drag, high-lift, and sonic boom prediction. While there are many factors that contribute to disagreement between simulated and experimental results, such as modeling or discretization error, quantifying the errors contained in a simulation is important for those who make decisions based on the computational results. The linearized error transport equations (ETE) combined with a truncation error estimate is a method to quantify one source of errors. The ETE are implemented with a complex-step method to provide an exact linearization with minimal source code modifications to CFD and multidisciplinary analysis methods. The equivalency of adjoint and linearized ETE functional error correction is demonstrated. Uniformly refined grids from a series of AIAA prediction workshops demonstrate the utility of ETE for multidisciplinary analysis with a connection between estimated discretization error and (resolved or under-resolved) flow features.

## I. Introduction

As the reliance on computational fluid dynamics (CFD) for making engineering decisions continues to grow, increased scrutiny is rightfully being directed toward the ‘correctness’ of the results produced by high fidelity CFD tools. This need is explicitly noted in the CFD Vision 2030 study,<sup>1</sup> where the ability to manage errors and uncertainties, whether from modeling errors, numerical errors, or from aleatory and epistemic uncertainties, is noted as a basic requirement for future CFD calculations. This shift from deterministic analysis to the inclusion of uncertainties is already underway so that risk management at the program level can be better informed.<sup>2</sup> This work acknowledges that even though a useful CFD result may be subject to many forms of error, there is benefit to using methods that quantify the numerical errors in a solution given a certain set of input parameters, modeling choices, and grid requirements. This effort for the identification, characterization, propagation, and analysis of error complements an update to the AIAA Guide for Verification and Validation of Computational Fluid Dynamics Simulations that is currently underway.<sup>3</sup> Oberkampf and Roy<sup>4</sup> list the errors that impact simulations and provide a detailed survey of discretization error estimation techniques. Mavriplis et al.<sup>5</sup> state, “Because discretization error has been identified as one of the leading sources of error for computational aerodynamics, improvement in the state of the art will require advances in grid generation technology, in addition to the development of new metrics and diagnostic tools.” The focus of this paper is on the quantification of discretization error, the difference between a computed discrete solution and the exact solution of the underlying governing equation(s), whether throughout a domain or with respect to a functional of interest.

---

\*Research Scientist, Computational AeroSciences Branch, 15 Langley Blvd. MS 128, AIAA Member

†Research Scientist, Computational AeroSciences Branch, 15 Langley Blvd. MS 128, AIAA Senior Member

‡Associate Research Fellow, 100 Exploration Way, Associate Fellow AIAA

Two forms of error estimation, the adjoint and error transport equation<sup>6</sup> (ETE) methods, are studied as implemented in the NASA unstructured mesh FUN3D software.<sup>7</sup> Besides providing a functional error estimate, adjoint methods can also be used to provide an indicator for grid adaptation, a necessary key for improving solution accuracy without resorting to uniform grid refinement or switching to a higher-order discretization scheme.<sup>8</sup> A functional error estimate can also be found through the use of the ETE. The ETE are related to adjoint methods, but since they provide local discretization error estimates, they can be used to compute an error estimate for any functional of interest at the cost of a single solution of the linear system. An exact implementation of the discrete, linearized ETE has recently been added to FUN3D through the use of the complex perturbation technique.<sup>9</sup>

This paper will discuss the theory and implementation of both the adjoint and ETE as well as the residual error estimate that drives them. In particular, the unique numerical tool that makes the exact implementation of the ETE possible will be discussed. Comparisons are made between the adjoint and ETE methods. Uniformly refined grid systems from the Drag Prediction Workshop (DPW),<sup>10</sup> High-Lift Prediction Workshop (HLPW),<sup>11</sup> and the Sonic Boom Prediction Workshop (SBPW)<sup>12</sup> show the utility of ETE to correct the solution to a refined grid solution.

## II. Error Transport Equations

The linearized ETE have seen limited use since they were first proposed, as they require the exact linearization of the underlying governing equations. In a series of papers, Cavallo et al.<sup>13–15</sup> have applied an approximate error transport formulation to solutions obtained from a variety of flow solvers, including USM3D and FUN3D. Phillips<sup>16</sup> and Derlaga<sup>17</sup> focused on the implementation and analysis of exact linearized ETE, adjoint equations, and defect correction methods. These works have recently been followed by the work of Tyson et al.<sup>18</sup> in which the equivalency between the adjoint and ETE error estimates noted by Derlaga<sup>17</sup> is formalized.

The ETE seek to estimate the discretization error, defined as the difference between the exact solutions of the underlying governing equations and their discrete surrogate, where the error is caused by the need to discretize and truncate the original governing equations. The Generalized Truncation Error Expression<sup>4</sup> (GTEE), Eq. (1), formalizes the well known relationship between the discrete approximation ( $L_h$ ) of the equations of interest ( $L$ ) given the truncation error introduced by the discretization process ( $\tau_h$ ), where  $u$  can be any function.

$$L_h(u) = L(u) + \tau_h(u) \quad (1)$$

If we define the exact solution to the continuous problem to be  $\tilde{u}$  and the exact solution to the discrete problem to be  $u_h$ , then the discretization error can be generally defined as:

$$\epsilon_h \equiv u_h - \tilde{u} \quad (2)$$

For finite-volume schemes,  $u_h$  exists only as an approximation of the average value of  $\tilde{u}$  over a computational cell. Therefore, the discretization error must also be thought of in terms of piecewise constant averages. Consider a control volume  $\Omega_i$ ; then the cell-averaged discretization error is defined as

$$u_{h_i} - \frac{1}{\Omega_i} \int \tilde{u} d\Omega_i = u_{h_i} - \bar{\tilde{u}} \equiv \bar{\epsilon}_h, \quad (3)$$

where an overbar denotes a cell average quantity. Alternatively, if a reconstruction of the discrete solution is used, then we have:

$$\epsilon_h = I_h u_h - \tilde{u}, \quad (4)$$

where  $I_h$  is a reconstruction operator from discrete to continuous space.

For both Eq. (3) and Eq. (4) to hold, the reconstruction operator must satisfy the conservation of the mean such that

$$\frac{1}{\Omega} \int (I_h u_h - \tilde{u}) d\Omega = u_{h_i} - \bar{\tilde{u}} \equiv \bar{\epsilon}_h, \quad (5)$$

and in the trivial case of  $I_h = 1$ , Eqs. 2, 3, and 4 are seen to hold.

If the restriction of the exact solution to the continuous governing equations is substituted into the GTEE of Eq. (1), and  $L_h(u_h) = 0$  is subtracted from both sides, we have:

$$L_h(I^h \tilde{u}) - L_h(u_h) = I^h \tau_h(\tilde{u}). \quad (6)$$

If we linearize  $L_h(I^h \tilde{u})$  about the discrete solution  $u_h$ , we have:

$$L_h(I^h \tilde{u}) = L_h(u_h) - \frac{\partial L_h}{\partial u_h} \epsilon_h + O(\|\epsilon_h\|^2), \quad (7)$$

which allows us to rewrite Eq. (6) (after some algebra) as the discrete, linearized ETE:

$$\frac{\partial L_h}{\partial u_h} \epsilon_h = -I^h \tau_h(\tilde{u}) + O(\epsilon_h^2) = I^h \tau_h(I_h u_h) + O(\epsilon_h^2), \quad (8)$$

where the TE is now approximated using the available discrete solution. This approximation can be made since, upon substitution of  $u_h$  into Eq. (1), we find that

$$L(I_h u_h) = -\tau_h(I_h u_h). \quad (9)$$

The Jacobian term in Eq. (8) should exactly linearize the discrete scheme that was used to solve for  $u_h$ . This can be costly to implement by hand for a comprehensive flow solver, therefore, the ETE are exactly implemented within the complex-variable version of the FUN3D code base.<sup>19</sup> Often used for the validation (or creation) of adjoint codes, the complex step method<sup>9</sup> uses an imaginary-number perturbation to evaluate derivatives to second-order accuracy. Complex step does not suffer from the cancellation errors of a real-valued finite difference, which allows the imaginary perturbation to be arbitrarily small. To the authors' knowledge, this is the first application of complex-step for implementing the ETE. As noted before, previous work has focused on hand differentiated<sup>16,17</sup> or approximated<sup>13</sup> Jacobians in order to implement the ETE, whereas the formulation in FUN3D avoids the tedium of (correctly) hand differentiating code or potential errors due to Jacobian approximations. Furthermore, the use of the complex step method guarantees the availability of discretization error estimates for any workflow path within FUN3D. This removes a limitation of FUN3D's hand-coded, adjoint-based error estimation, where only a subset of all the capabilities have been differentiated by hand. Once the complete Jacobian matrix is formed, Eq. (8) can be solved with a time marching approach instead of through direct inversion:

$$\left[ \frac{\Omega}{\Delta t} I + \frac{\partial L_h}{\partial u_h} \right] \Delta \epsilon_h^n = -\frac{\partial L_h}{\partial u_h} \epsilon_h^n + I^h \tau_h(I_h u_h), \quad (10)$$

where the Jacobian on the left side of the equation can be approximated to a lower order than the Jacobian matrix on the right side of the equation to reduce the cost associated with solving the linear system. The complex-valued solver naturally performs this time advancement of the imaginary perturbation by using the standard flow solution scheme with complex-valued arithmetic.

### III. Adjoint Method

The adjoint solution can be used as an alternative to ETE, but only for estimating error in a functional. Consider a discrete functional  $J_h(u_h)$ , which has a Taylor series expansion about the restricted exact solution  $\tilde{u}$  of:

$$J_h(u_h) = J_h(\tilde{u}) + \frac{\partial J_h}{\partial u_h}(u_h - \tilde{u}) + \frac{\partial^2 J_h}{\partial u_h^2} \frac{(u_h - \tilde{u})^2}{2} + \dots \quad (11)$$

If we were to truncate this Taylor series and combine it with a truncated Taylor series expansion of our discrete problem  $L_h(u_h) = 0$ , we could combine the expansions via a Lagrangian:

$$\begin{aligned} J_h(u_h) \approx & J_h(\tilde{u}) + \frac{\partial J_h}{\partial u_h}(u_h - \tilde{u}) + \frac{\partial^2 J_h}{\partial u_h^2} \frac{(u_h - \tilde{u})^2}{2} \dots \\ & + \lambda_h \left[ L_h(\tilde{u}) + \frac{\partial L_h}{\partial u_h}(u_h - \tilde{u}) + \frac{\partial^2 L_h}{\partial u_h^2} \frac{(u_h - \tilde{u})^2}{2} \right], \end{aligned} \quad (12)$$

where  $\lambda_h$  is currently undefined. Since we know that  $u_h - \tilde{u} = \epsilon_h$ , we can rearrange Eq. (12) to be:

$$J_h(u_h) \approx J_h(\tilde{u}) + \lambda_h L_h(\tilde{u}) + \epsilon_h \left[ \frac{\partial J_h}{\partial u_h} + \lambda_h \frac{\partial L_h}{\partial u_h} \right] + \frac{\epsilon_h^2}{2} \left[ \frac{\partial^2 J_h}{\partial u_h^2} + \lambda_h \frac{\partial^2 L_h}{\partial u_h^2} \right]. \quad (13)$$

We can now substitute the truncation error by use of Eq. (9):

$$J_h(u_h) \approx J_h(\tilde{u}) + \lambda_h \tau_h(\tilde{u}) + \epsilon_h \left[ \frac{\partial J_h}{\partial u_h} + \lambda_h \frac{\partial L_h}{\partial u_h} \right] + \frac{\epsilon_h^2}{2} \left[ \frac{\partial^2 J_h}{\partial u_h^2} + \lambda_h \frac{\partial^2 L_h}{\partial u_h^2} \right]. \quad (14)$$

To this point,  $\lambda_h$  is still undefined, but we choose to solve the adjoint problem given by the third term of the right side of Eq. (14) in order to remove the first-order influence of the discretization error on the functional estimate, yielding:

$$\lambda_h = - \left[ \frac{\partial J_h}{\partial u_h} \right] \left[ \frac{\partial L_h}{\partial u_h} \right]^{-1} \quad (15)$$

Once the adjoint solution has been determined, we find that Eq. (14) reduces to the standard adjoint functional correction equation:

$$J_h(\tilde{u}) = J_h(u_h) - \lambda_h \tau_h(\tilde{u}) + O(\epsilon_h^2), \quad (16)$$

which in turn can be rewritten as

$$J_h(\tilde{u}) = J_h(u_h) + \left[ \frac{\partial J_h}{\partial u_h} \right] \left[ \frac{\partial L_h}{\partial u_h} \right]^{-1} \tau_h(\tilde{u}) + O(\epsilon_h^2). \quad (17)$$

At this point, we note that Eq. (11) can be rewritten in a similar manner to Eq. (17) as:

$$J_h(\tilde{u}) = J_h(u_h) - \frac{\partial J_h}{\partial u_h} \epsilon_h + O(\epsilon_h^2), \quad (18)$$

where from the linearized ETE,

$$\epsilon_h = - \left[ \frac{\partial L_h}{\partial u_h} \right]^{-1} \tau_h(\tilde{u}), \quad (19)$$

and therefore the same functional discretization error estimate is obtained from either the adjoint error correction or linearized ETE as long as the same truncation error estimate is used, as discussed in Derlaga<sup>17</sup> and Tyson et al.<sup>18</sup> This means that for the cost of a single solution of the linearized ETE, any functional error estimate can be obtained that matches the result obtained via the adjoint method. However, since the adjoint method requires the solution of one right-hand-side operator per functional, the ETE method has a lower overall cost for multiple functionals as it only depends on the solution of a single right-hand-side problem.

## IV. Implementation of Error Transport Equations

FUN3D is a node-centered, edge-based, fully unstructured finite-volume solver, which has been under continuous development at NASA Langley for several decades.<sup>7</sup> FUN3D provides a complex-valued version through a script that appropriately replaces real-valued variables and functions with complex number forms.<sup>19</sup> The complex-valued version of FUN3D was originally developed to provide sensitivity derivatives<sup>9,20</sup> and to verify the correctness of the hand-coded discrete adjoint implementation.<sup>21</sup>

A derivative is obtained with respect to a given variable by seeding an imaginary perturbation to that variable. For example, an angle of attack derivative is obtained by adding an imaginary perturbation to the far-field boundary conditions. This complex-valued perturbation propagates throughout the solution and can be used to obtain derivatives for any functional or the entire solution field. In this manner, a second-order accurate calculation of the residual Jacobian can be obtained, which is necessary to solve the ETE problem.

To drive the ETE solver, the residual of the complexified solver is given an imaginary number perturbation of the truncation error estimate scaled by double precision epsilon (smallest difference that can be represented near zero). The use of double precision epsilon assumes the local absolute values of truncation error estimate



are much smaller than one. If the truncation error estimate is locally larger than one, use a smaller epsilon to keep the product of epsilon and the truncation error estimate small to avoid errors in the sensitivity calculation. The imaginary part of the complex solution (and functional outputs) is divided by the epsilon used to scale the imaginary truncation error source term to compute the ETE correction of the entire solution (and functionals).

The workflow for obtaining an ETE solution consists of two parts: (1) run the real-valued solver to obtain a flow solution and truncation/residual error estimate, and (2) run the complex variable solver. Running the real-valued solver is performed in the same fashion as any other study with FUN3D, but to obtain a residual error estimate and export it to file by reusing the parallel adjoint-based error estimate mechanics,<sup>22</sup> the following option is added to the FUN3D namelist input file.<sup>7</sup>

```
&adapt_metric_construction
  adapt_export_truncation_error = .true.
/
```

To solve the ETE problem, the complex-valued solver is run with the real-valued restart flow file and the truncation error estimate file. Because the solution has already been converged fully or partially by the real-valued solver, only the imaginary part of the complex-valued solution needs to be obtained. This eliminates solution robustness issues related to poorly chosen initial conditions. Due to the complex variable method used to form the ETE solver, this process can be used for all analysis capabilities in FUN3D, i.e., it is not limited to the subset of FUN3D where the hand-coded adjoint is available.

#### IV.A. Residual Error Estimate

To this point, no details have been given on exactly how a truncation error estimate can be obtained. Since most simulations are performed where no exact solution to the continuous equations is known, most truncation error estimates must be based on the discrete solution. These error estimation methods make the assumption that the primal solution is converged (primal residual is negligible). Any remaining iterative error in the solution scheme can pollute these truncation error estimates. Pierce and Giles,<sup>23</sup> Phillips,<sup>16</sup> Derlaga,<sup>17</sup> and Yan and Gooch<sup>24</sup> have all sought TE estimates by creating continuous or piecewise continuous reconstructions of the discrete solution and applying the continuous operator  $L$  to the reconstruction. The overall goal of this approach is to obtain a  $p^\#$  (p-sharp) error estimate, where for uniformly refined grids, the error estimate results in a convergence of the remaining error which is twice that of the formal order ( $p$ ) of the underlying discretization.

An alternative approach seeks to provide an  $h^\#$  (h-sharp) error estimate, where instead of an increase in the convergence rate of the error estimate, the error estimate provides an a priori estimate of the solution on a finer grid. This is accomplished by reconstructing the solution from a given mesh onto a finer mesh, and then applying the discrete operator on the finer mesh. The residual can then be restricted to the original mesh to serve as a source term for the ETE solver. Alternatively, an adjoint solution from the current mesh can be combined with the finer grid residual to provide an improved functional error estimate. The latter is the approach originally used by Venditti and Darmofal<sup>25-27</sup> and currently implemented within FUN3D.<sup>28,29</sup> Due to how FUN3D exports the truncation error estimate as an input to the ETE solver, the current process is compatible with any form of  $p^\#$  truncation error estimate when it becomes available in FUN3D.

#### IV.B. Strong Boundary Conditions

FUN3D uses strong boundary conditions for no slip and symmetry boundary conditions. Strong boundary conditions explicitly specify some, or all, of the solution at boundary nodes<sup>30</sup> rather than solving the underlying governing equations. The replacement of the governing equation with the strong Dirichlet statement changes the characteristic of the discrete adjoint (and the ETE).<sup>31</sup> Venditti<sup>27</sup> provides further discussion of the strong boundary conditions in FUN3D and implications for error estimation via adjoint solution reconstruction on embedded grids.

While the reconstruction scheme used by FUN3D to form the embedded grid residual error estimate respects the strong enforcement of the boundary conditions,<sup>32</sup> for this study, the truncation error estimate is set to zero for nodes and equations with strong boundary conditions. This is interpreted as the strong boundary conditions being satisfied exactly despite the behavior of the interior cells. Including terms that fully account for errors in specifying the strong boundary conditions is left as a topic for future work.

## IV.C. Multidisciplinary Sonic Boom Analysis

The linearized ETE method implemented in FUN3D is also applicable to coupled multidisciplinary analysis. Sonic boom prediction is a multidisciplinary analysis that involves near-field CFD and atmospheric propagation. The implementation of sonic boom ETE is provided as a single example of this class of complex coupled analysis. The sonic boom analysis process is described here to provide details for an example of sonic boom ETE in the results section.

Evaluation of the loudness footprint of an aircraft concept involves a multi-step process<sup>33</sup> that begins by calculating the pressure field around an aircraft by using a CFD solver. A near-field pressure signature is extracted from the CFD solution and propagated to the ground. An augmented Burgers' equation solver sBOOM<sup>34</sup> is used for atmospheric propagation. Noise measures are calculated from the ground signature.<sup>35</sup> In previous work, a discrete adjoint formulation for this process was created for design optimization,<sup>36</sup> where the coupling between CFD and propagation tools allows computation of A-weighted Sound Exposure Level (ASEL) sensitivities to underlying mesh and geometry parameters. A complex-valued version of sBOOM was created to aid adjoint development and verify exactness.<sup>36</sup> The complex-valued sBOOM is used in this work by propagating a complex pressure signature obtained from FUN3D. The pressure signature consists of both the real-valued near-field pressure signature obtained by the baseline solver and the imaginary-valued error estimate of the pressure signature obtained from the FUN3D ETE solver.

ASEL is a good surrogate for the subjective experience of sonic boom annoyance because it is highly correlated to human response data.<sup>37</sup> The ASEL noise measure can be computed in the frequency domain<sup>35</sup> or time domain.<sup>38</sup> Both approaches yield identical results. A time domain formulation is implemented in sBOOM, because it is easier to hand differentiate for the adjoint formulation.<sup>36</sup> The complex-valued ground signature is provided to the noise measure calculation method to produce a complex-valued ASEL.

This multidisciplinary approach combines the disciplines of CFD, atmospheric propagation, and noise measure calculation. Other forms of multidisciplinary analysis could be accommodated in this error estimation procedure such as aero-propulso-servo-elasticity.<sup>39,40</sup> A coupled analysis with an available tangent or complex-valued solver (see Mishra et al.<sup>41</sup>) could readily be extended to include ETE.

## V. Conditions for Error Estimate Utility

An important concern, as discussed by Cavallo and Sinha,<sup>13</sup> is that an error estimate will only be accurate if the flow field is properly resolved. Both the adjoint equations and ETE are based on a linearization about the currently computed solution. If the solution is under-resolved, then the appropriateness of the linearization is suspect, and the error estimates may be misleading by not representing the true continuous governing equations. If a feature, such as a shock, is not present or has dissipated before it has reached the far field, an appropriate truncation or residual error estimate is not computable. Under-resolved flow features can lead to false confidence in the computed error estimates and can require a human to interpret whether an error estimate actually makes sense. An example of this can be seen in the work of Park,<sup>42</sup> where the functional of interest, a far-field pressure integral, would initially appear to be accurately captured based on the adjoint error estimate. However, since the flow is under-resolved, the validity of the error estimation model is in question, and grid adaptation is required to obtain a true sense of the discretization error.<sup>43</sup> To address these concerns, output-based adaptive error indicators typically target the remaining nonlinear sources of error after a linear correction is applied.<sup>8</sup> Norm-oriented mesh adaptation<sup>44</sup> is another approach to improve the linear correction. The discretization error itself should not be targeted for adaptation; it is simply a symptom of the problems caused by the truncation error.

In general, the root cause of poor error estimates is difficult to determine; a better resolved flow field in these regions may result in a better solution around which to linearize or create a truncation error estimate, or the ETE may not be capable of accurately accounting for various nonlinearities even with a well resolved flow field. One potential method to help clarify this issue is the use of the defect correction method,<sup>32</sup> which uses the truncation error estimate as a source term in the original, nonlinearized, system; another is the nonlinear ETE as discussed in Banks et al.<sup>45</sup> and Yan and Gooch.<sup>24</sup>

## VI. Results

A range of AIAA prediction workshop cases are analyzed to show the utility of this approach and how ETE can compliment uniform grid refinement studies. The ETE solution is shown as a correction to line plots and as a scalar field for surface plots. Cavallo, O’Gara and Schikore<sup>46</sup> present alternative visualization techniques for their ETE solution, which has a magnitude rather than a signed correction. Calculations on uniformly-refined grids are presented to show discretization error trends. The benefits of having a numerical and visual description of the errors inherent in a computational simulation is demonstrated by a discussion of physical processes correlated with large corrections. The purpose of this method is to quantify and correct discretization error. Experimental measurements are not presented because the difference between computed and measured data would also include modeling and other forms of error.

### VI.A. Adjoint ETE Equivalence: Gaussian Bump

Before examining the various AIAA Prediction Workshop cases, several simpler cases were studied to ensure the correct implementation of the ETE solver. One such example is isentropic flow over a Gaussian bump with weakly enforced boundary conditions, as shown in Fig. 1. The grid is shown in Fig. 1(a). The reference Mach number is 0.38 and the distribution of Mach number is shown in Fig. 1(c). Examining a lift functional for the bottom wall of the channel, the lift correction from the ETE solution is 0.0100876927761275 and the adjoint correction is 0.0100876927761291, which differ in the last two digits by  $1.6 \times 10^{-15}$ . This difference is within round-off error of double precision floating point operations. These correspond to the equivalent terms  $\frac{\partial J_h}{\partial u_h} \epsilon_h$  in Eq. (18) for the ETE method and  $\lambda_h \tau_h(\tilde{u})$  in Eq. (16) for the adjoint method.

Examining the solutions obtained by both methods, the density correction, the imaginary-valued quantity obtained from the ETE solver, is shown in Fig. 1(b) and the adjoint variable corresponding to the continuity equation is shown in Fig. 1(d). The adjoint variables can be difficult to interpret, but can be viewed as linear sensitivities that reflect the domain of dependence of a functional on a local source term to the governing equations; in this case, the functional is the lift on the bottom wall of the channel. Clearly, the regions upstream of the bump and on top of the bump are extremely important to the lift functional. In contrast, the density error from the ETE solver shows the actual buildup of error which begins in front of the bump as well as the error which streams off the leeward side. Essentially, the adjoint solution indicates where it is important to accurately simulate a flow, while the ETE solution gives insight into what errors exist in a computed solution. With the equivalency between the adjoint and ETE methods within FUN3D being demonstrated, we can now apply the ETE solver to the various workshop cases.

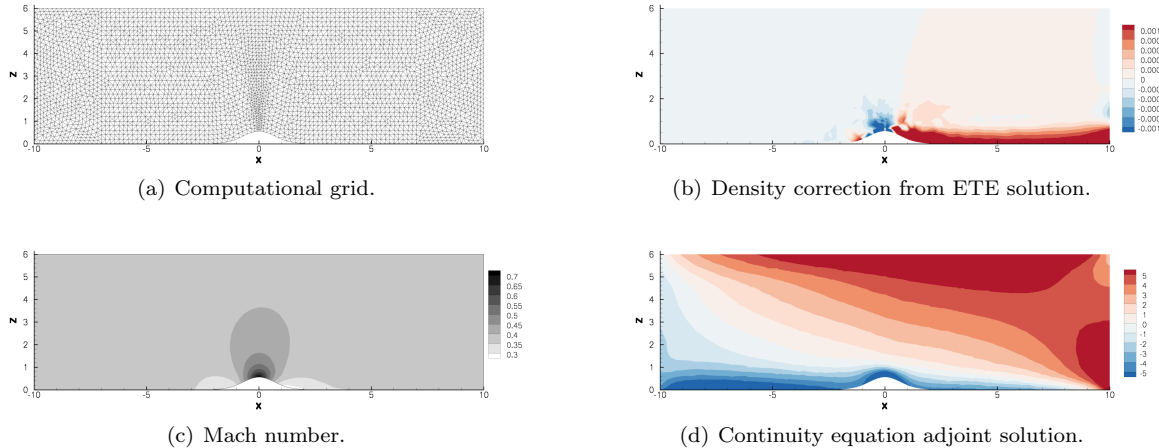


Figure 1. Gaussian bump channel test case.

## VI.B. 6<sup>th</sup> AIAA CFD Drag Prediction Workshop

The viscous transonic configuration of Case 3 of the 6<sup>th</sup> AIAA CFD Drag Prediction Workshop (where the wing-body geometry reflects static aero-elastic effects) is studied at an angle of attack of 2.75 degrees, at a Mach number of 0.85. The pressure coefficient on a coarse grid level is shown in Fig. 2, and the ETE correction term in Fig. 3. The shock on the wing is clearly marked as a localized region of high error, within an order of magnitude of the flow solution, while most of the error on the rest of the body are approximately two orders of magnitude lower than the flow solution. The negative error estimate in the captured shock can be interpreted as a correction to move the shock location farther aft on the wing, to a position which matches that of the next finer grid level, as shown in Fig. 4. Obtaining the proper shock location is critical to properly estimating the drag on the wing and ensuring that extra errors associated with the wrong shock jump conditions are not propagated farther down stream. Also visible in Fig. 3 is the error related to the scrubbing from a horse-shoe vortex in front of the wing and trailing along the wing/fuselage junction fairing, a region where unsteadiness may occur. In addition, geometric discontinuities such as the wing trailing edge fuselage juncture and the horizontal tail mounting plane show localized regions of large correction to coefficient of pressure. A key benefit of the ETE method is the ability to visualize the effects of error on aerodynamic surfaces. This can help designers to place new components or make other changes to the configuration in locations where uncertainty due to discretization error is low.

The total lift, drag, and pitching moment coefficients are listed in Table 1. The number of nodes for each grid is listed for the flow and ETE solution. The number of nodes in the embedded grid for the  $h^\#$  truncation error estimate is listed in parenthesis. The ETE solver uses the same number of nodes as the flow solver. The embedded grid is only used to evaluate one residual with an interpolated solution to form the truncation error estimate. With the exception of drag, the corrected functional predicts the direction of the discretization error between the coarse and medium grids.

Table 1. DPW-6 forces and moment.

case	nodes (embedded)	$C_L$	$C_D$	$C_m$
coarse	29,927,558	0.495	0.0256	-0.0716
coarse ETE	(236,096,336)	0.500	0.0256	-0.0756
medium	44,263,902	0.502	0.0259	-0.0766

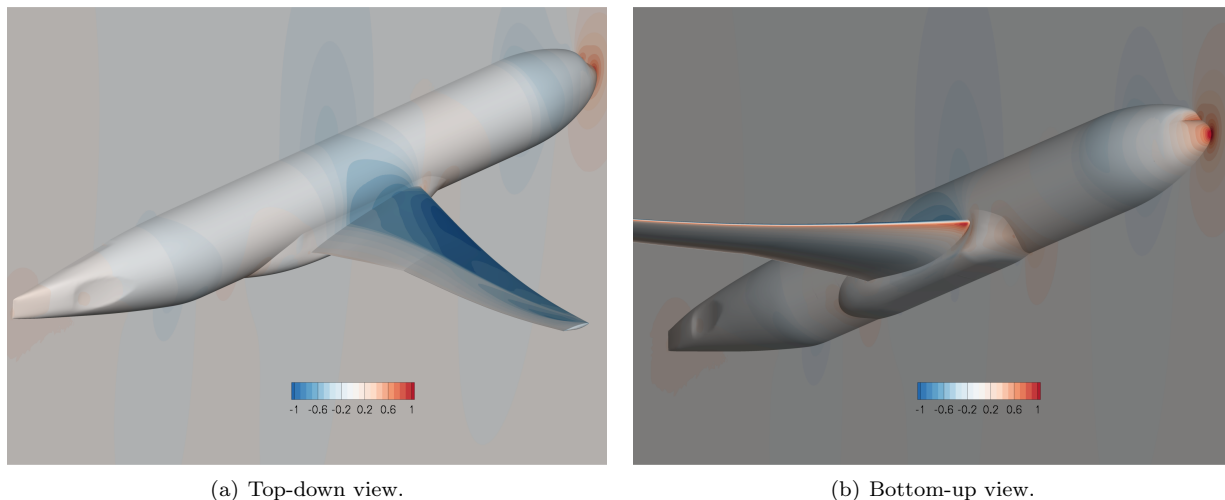
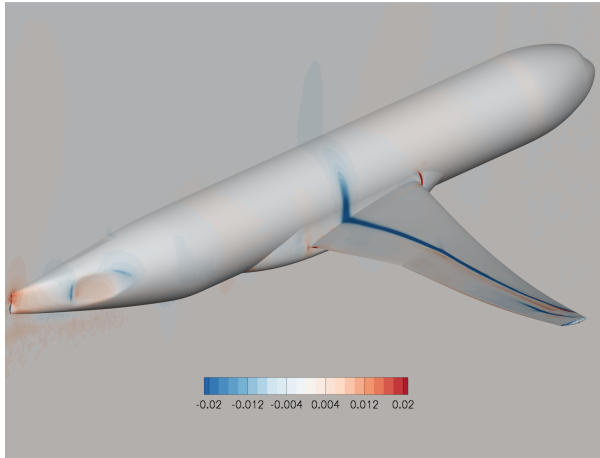
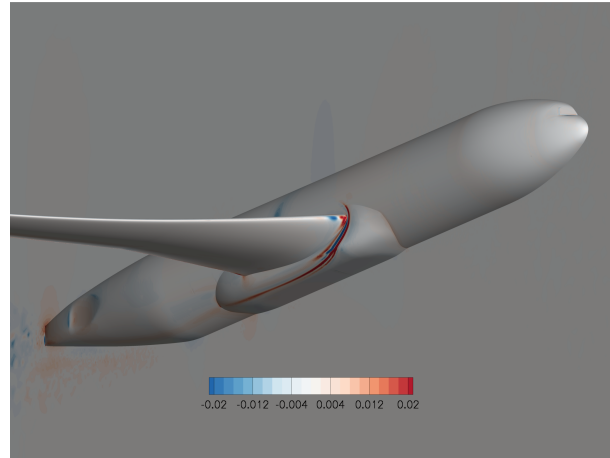


Figure 2. DPW-6 coefficient of pressure,  $\alpha = 2.75$ , coarse grid.



(a) Top-down view.



(b) Bottom-up view.

Figure 3. DPW-6 coefficient of pressure ETE solution,  $\alpha = 2.75$ , coarse grid.

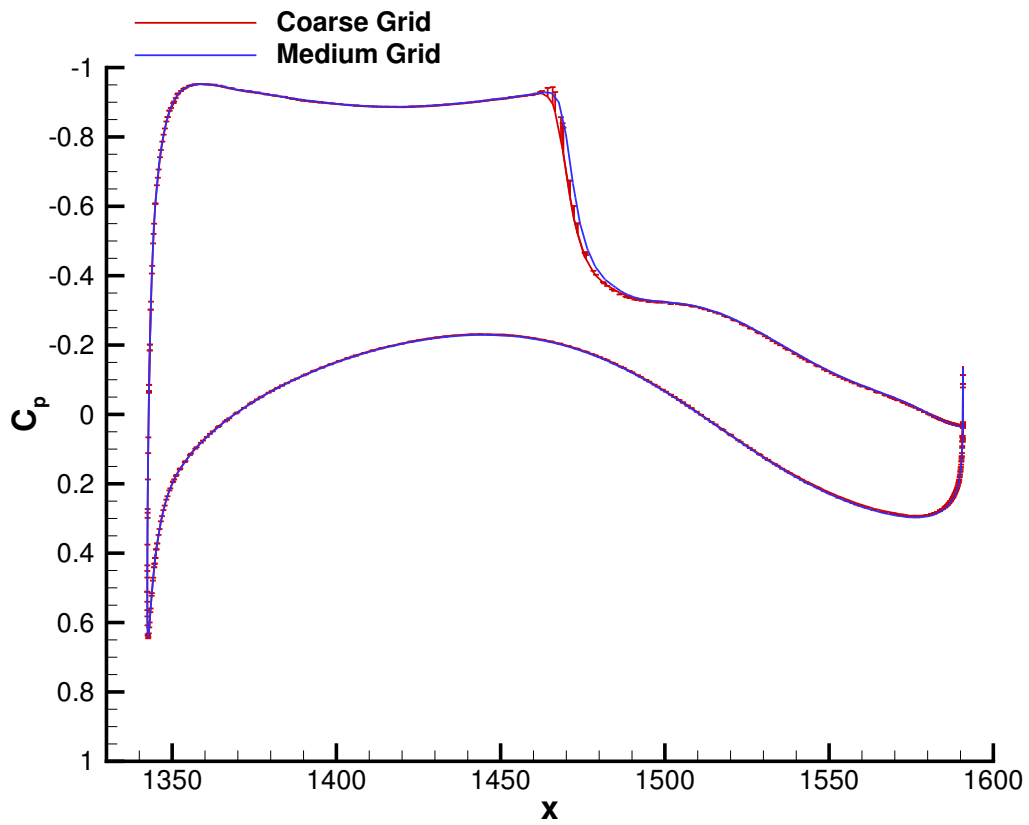


Figure 4. DPW-6 coefficient of pressure slice at wing station 10,  $\eta = 0.5024$ .

## VI.C. 1<sup>st</sup> AIAA CFD High Lift Prediction Workshop

The Trap Wing configuration 1 of the 1<sup>st</sup> AIAA CFD High Lift Prediction Workshop<sup>47</sup> is presented here in a similar manner as the approximate ETE method of Cavallo et al.<sup>14</sup> to facilitate comparison between the methods. Semi-span ( $\eta$ ) wing slices of the pressure coefficient at 13 degrees angle of attack for the coarse, medium, and fine node-based tetrahedral grids are shown in Fig. 5 for  $\eta = 0.85$  and Fig. 6 for  $\eta = 0.95$ . These are the same conditions and constant spanwise locations as Fig. 18 of Cavallo et al.<sup>14</sup> One immediate difference is that the present approach treats the ETE solution as an  $h^\#$  error correction, which is rendered as a one-sided error bar. In regions of the flow field where there is attached flow on the slat, wing, and flap, the corrected solution is seen to approach the solution on the next finer mesh in an  $h^\#$  manner. In regions where flow separation occurs, such as on the aft section of the flap, or other highly nonlinear flow features, such as the wing tip vortex, the linearized ETE may not be able to properly account for the true behavior of the nonlinear discretization error.

As some geometric features become better resolved, such as the curvature at the fuselage side to its upper and lower surfaces, the error in these regions is reduced, as seen in Fig. 7 and Fig. 10. However, the error does not reduce uniformly with grid refinement. As shown in Fig. 7(e) and (f), side of body separation becomes important and results in a wake of error which is convected down stream. In addition, the sign of the error on the suction side of the flap changes with grid refinement as well, and seems to be correlated with the sign of the error of the wing tip vortex on the main element. As the grid is refined, the effects of certain flow features can be better seen, such as the horseshoe vortex at the junction of the slat and the fuselage.

In a seemingly counter intuitive manner, the results at 28 degrees angle of attack, Fig. 8 for  $\eta = 0.85$  and Fig. 9 for  $\eta = 0.95$ , indicate that the ETE solution is performing in a more  $h^\#$  manner than the correction obtained at 13 degrees angle of attack. However, the higher angle of attack case is more representative of the true design point of the geometry and experiences less separation at the slat, producing less error that is propagated downstream as compared to the lower angle of attack. However, side of body separation at the flap is still seen to impact the solution.

The total lift, drag, and pitching moment coefficients are listed in Table 2 for  $\alpha = 13$  degrees and Table 3 for  $\alpha = 28$  degrees. The number of nodes for each grid is listed for the flow and ETE solution. The number of nodes in the embedded grid for the  $h^\#$  truncation error estimate is listed in parenthesis. The ETE solver uses the same number of nodes as the flow solver. As for the DPW-VI case, the embedded grid is only used to evaluate one residual with an interpolated solution to form the truncation error estimate. The ETE forces and moment predict the trends seen with grid refinement. The grid refinement trends of the flow solver and ETE appear to be converging.

**Table 2. Trap Wing forces and moments,  $\alpha = 13$  degrees.**

case	nodes (embedded)	$C_L$	$C_D$	$C_m$
coarse	3,652,657	1.873	0.3194	-0.4286
coarse ETE	(28,936,013)	1.927	0.3153	-0.4356
medium	10,957,783	1.965	0.3190	-0.4568
medium ETE	(86,686,629)	2.014	0.3267	-0.4804
fine	32,297,530	1.986	0.3227	-0.4723
fine ETE	(255,300,571)	2.012	0.3319	-0.4760

**Table 3. Trap Wing forces and moments,  $\alpha = 28$  degrees.**

case	nodes (embedded)	$C_L$	$C_D$	$C_m$
coarse	3,652,657	2.637	0.6419	-0.3743
coarse ETE	(28,936,013)	2.900	0.6814	-0.4169
medium	10,957,783	2.849	0.6704	-0.4256
medium ETE	(86,686,629)	2.913	0.6828	-0.4515
fine	32,297,530	2.888	0.6756	-0.4450
fine ETE	(255,300,571)	2.909	0.6833	-0.4519

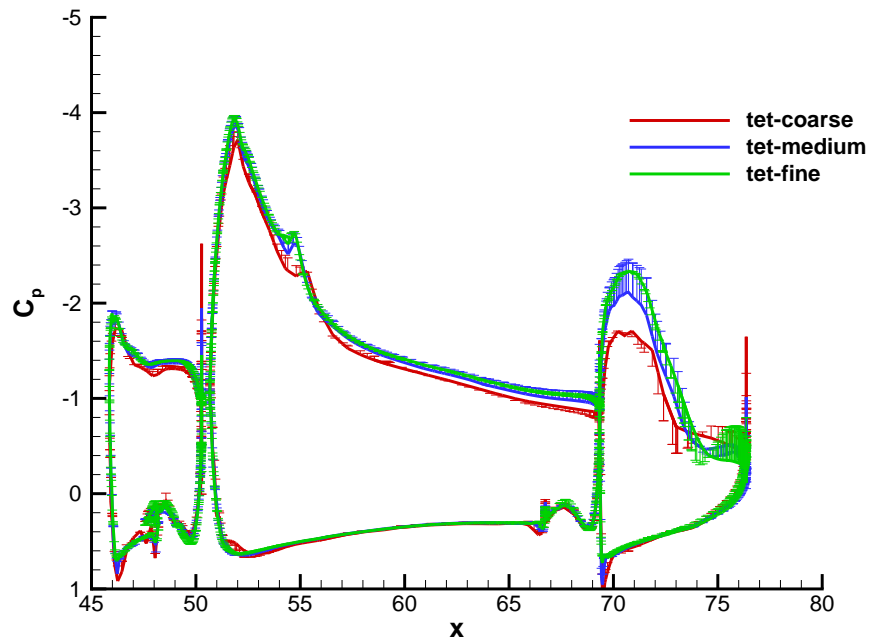


Figure 5. Trap Wing coefficient of pressure and ETE solution,  $\alpha = 13$  degrees,  $\eta = 0.85$ .

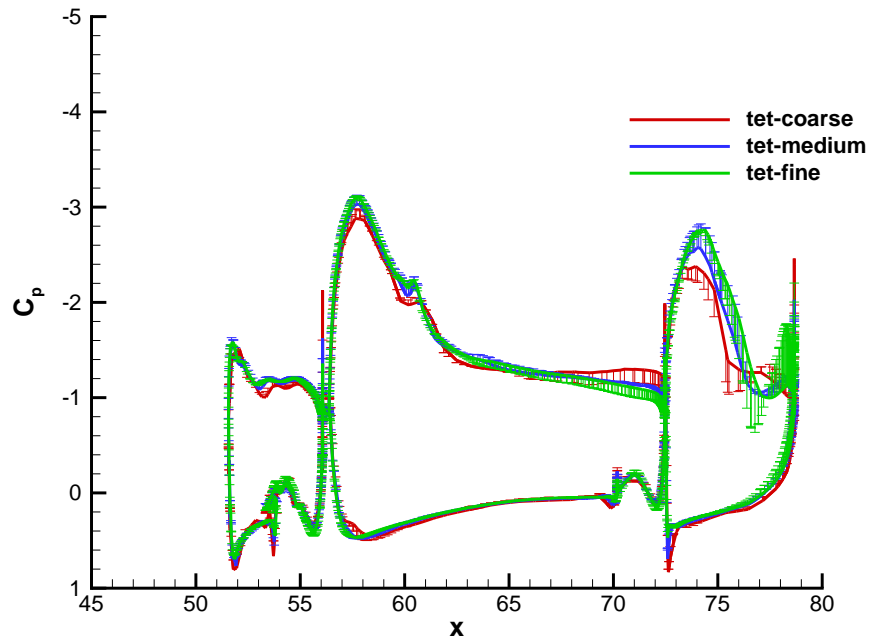
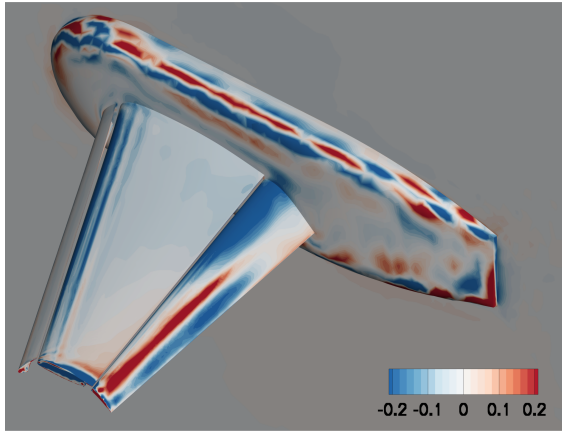
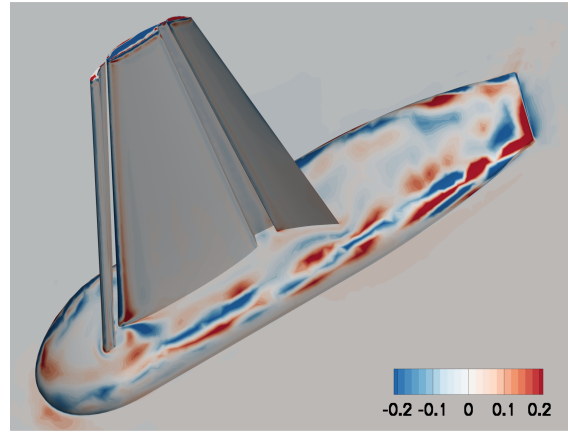


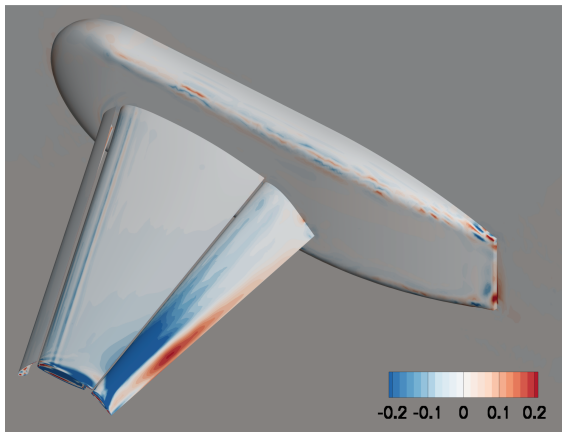
Figure 6. Trap Wing coefficient of pressure and ETE solution,  $\alpha = 13$  degrees,  $\eta = 0.95$ .



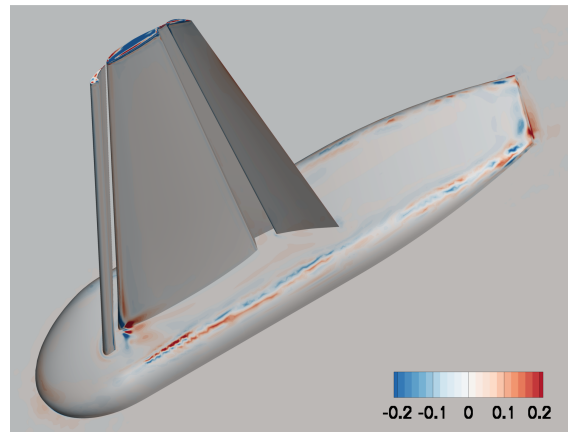
(a) Top-down view, coarse grid.



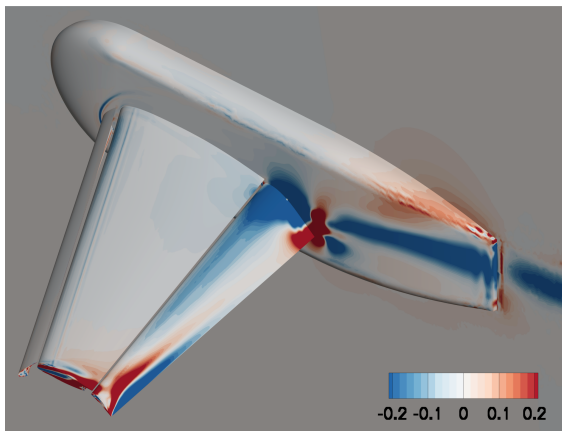
(b) Bottom-up view, coarse grid.



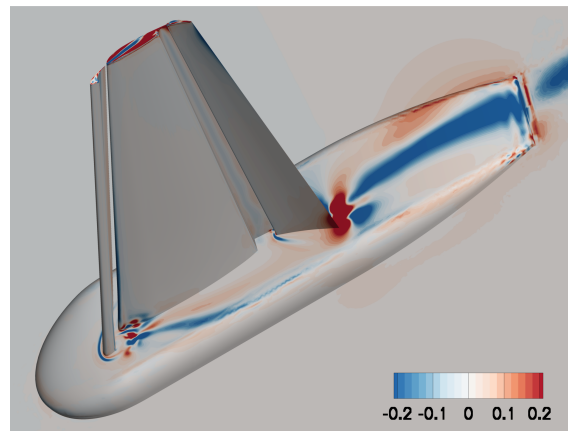
(c) Top-down view, medium grid.



(d) Bottom-up view, medium grid.



(e) Top-down view, fine grid.



(f) Bottom-up view, fine grid.

**Figure 7. Trap Wing coefficient of pressure ETE solution,  $\alpha = 13$  degrees.**



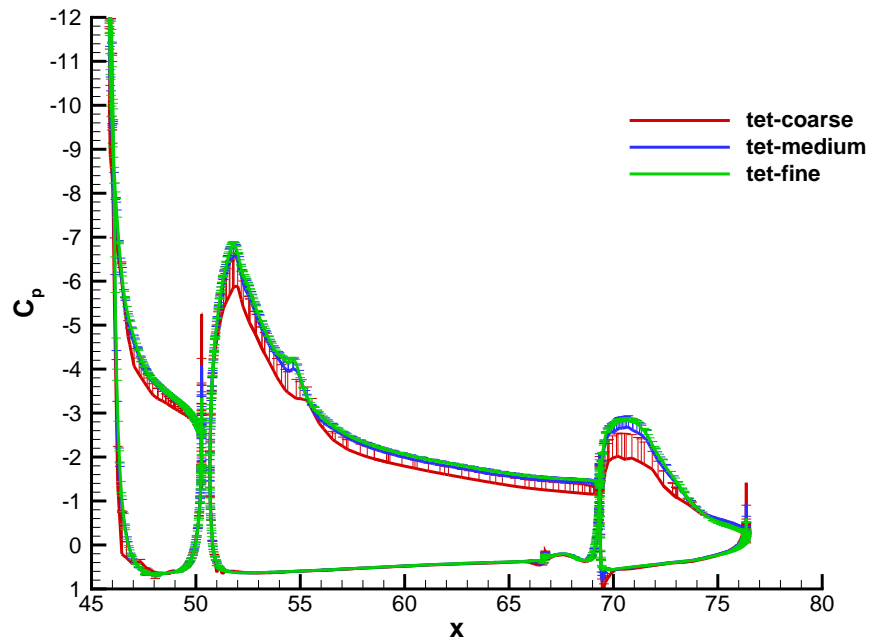


Figure 8. Trap Wing coefficient of pressure and ETE solution,  $\alpha = 28$  degrees,  $\eta = 0.85$ .

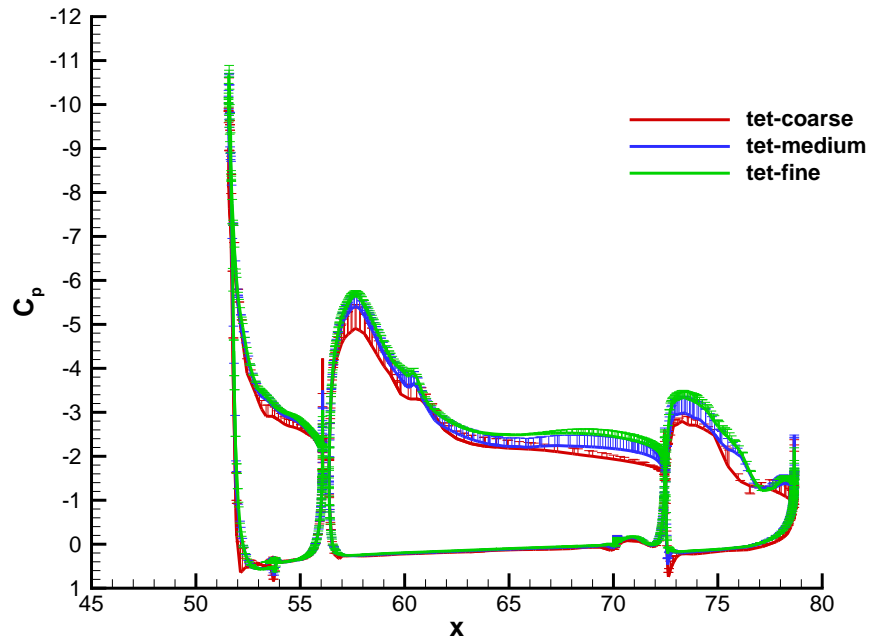
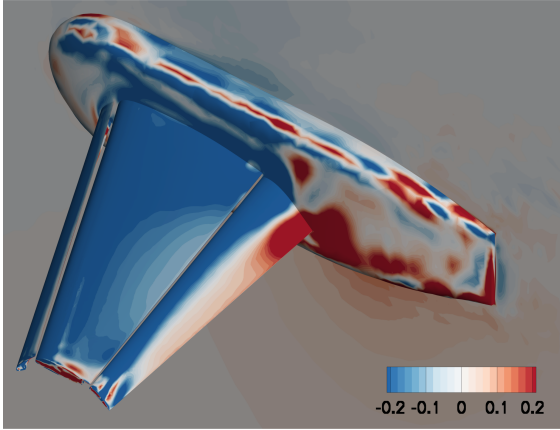
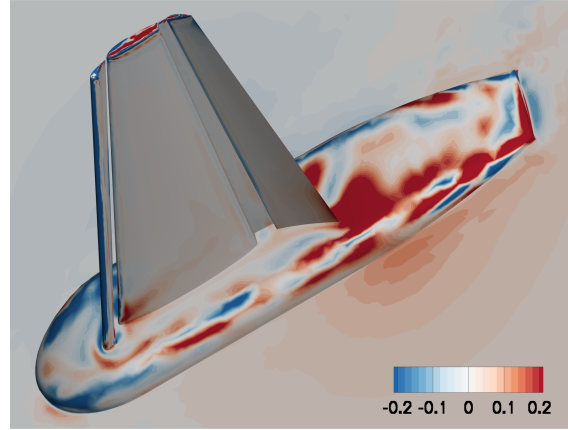


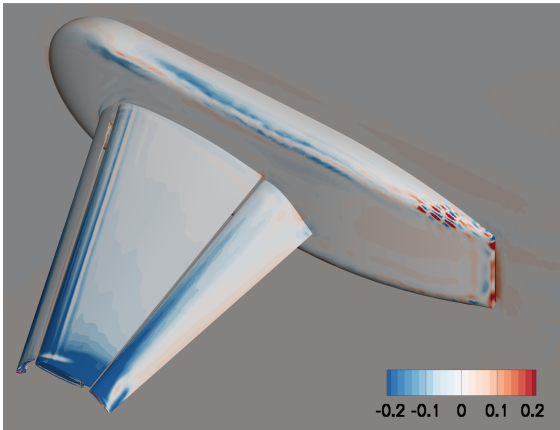
Figure 9. Trap Wing coefficient of pressure and ETE solution,  $\alpha = 28$  degrees,  $\eta = 0.95$ .



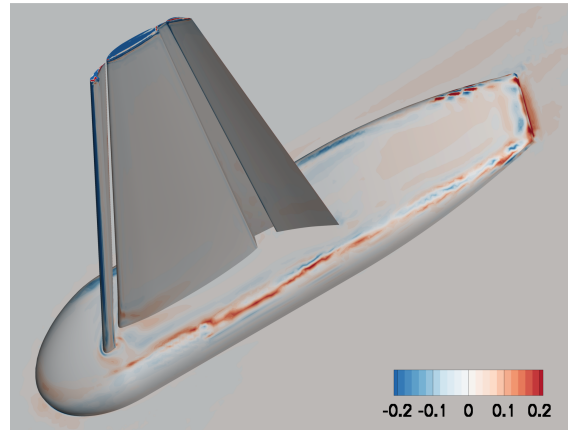
(a) Top-down view, coarse grid.



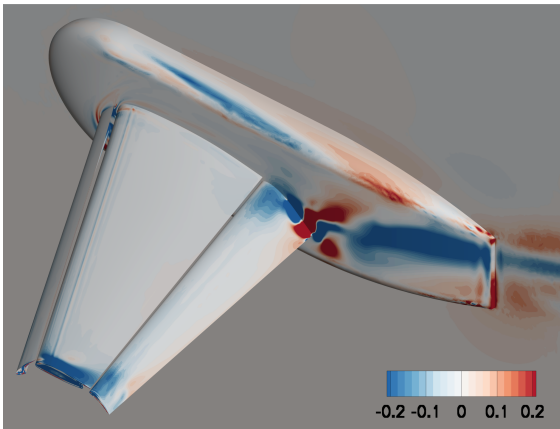
(b) Bottom-up view, coarse grid.



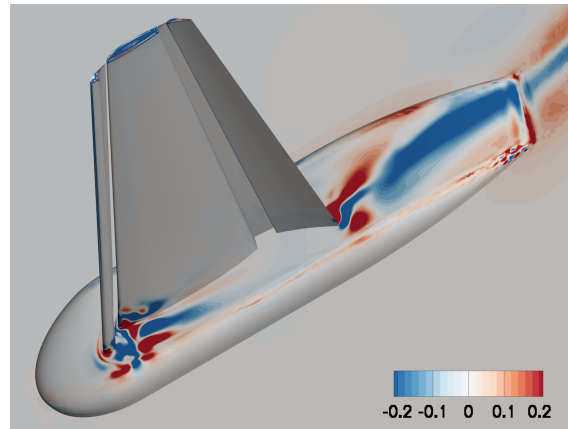
(c) Top-down view, medium grid.



(d) Bottom-up view, medium grid.



(e) Top-down view, fine grid.



(f) Bottom-up view, fine grid.

**Figure 10. Trap Wing coefficient of pressure ETE solution,  $\alpha = 28$  degrees.**

## VI.D. 2<sup>nd</sup> AIAA Sonic Boom Prediction Workshop

The C25D is a notional configuration created to represent a sonic boom demonstrator class vehicle. This model includes wing, body, tail, nacelle, and flow through engine path. It was designed primarily for a low ground loudness measure near the centerline of the flightpath,<sup>48</sup> with some reduction in the noise measure over the entire boom carpet.<sup>49</sup> The Euler CFD method Cart3D was used to design the configuration, as described by Wintzer.<sup>50</sup>

This configuration is a required case for the 2<sup>nd</sup> AIAA Sonic Boom Prediction Workshop. The geometry was created using an OpenCSM<sup>51</sup> script based on the Jaguar<sup>50</sup> description used to design the model. The OpenCSM model is not a perfect recreation of the Jaguar model. The OpenCSM nacelle outer model line is linearly interpolated between fuselage stations where the Jaguar model is splined. There are other smaller known differences that result in different loudness measures in this analysis than the references describing the design.<sup>48,49</sup> The geometry and grid systems provided by the workshop have been rotated to include the design angle of attack of 3.375 degrees. The freestream Mach number is 1.6. The grid generation approach of Park et al.<sup>52</sup> was used to create a family of uniformly refined mixed-element grids intended for Euler analysis. The unstructured sequence of grids was generated with a spacing field that decreases by factors of approximately 0.8, see Table 4.

Table 4. C25D grid sizing.

$h$	nodes	tetrahedra	prisms
2.00	3,419,776	5,564,030	4,810,500
1.60	6,323,343	10,327,822	8,918,375
1.28	13,083,168	20,317,100	18,921,920
1.00	26,923,206	42,433,653	38,890,800
0.80	51,542,500	82,620,767	74,194,500

The near-field pressure signature at one body length below the configuration on the centerline is shown in Fig. 11. The signature for five grid levels are shown as lines. The one sided error bars depict the ETE correction for the four coarsest grids. The maximum size of the queue on the machine used for this study limited the memory available, which prevented forming the embedded grid for the truncation error estimate on the finest grid. An alternative truncation error estimate formulation could reduce the memory required. The truncation error estimate for the linear ETE is calculated on an embedded grid which has an average edge length of one half of the original grid, i.e., the  $h = 2.00$  error correction should represent the  $h = 1.00$  solution under ideal conditions.

The correction is smaller in the forward portion of the signature than the aft portion of the signature. The smoother portions of the signature indicate that in the smoother portions of the signature, coarse grid solutions plus the error correction converge toward the finer grid solutions. Some portions of the signature have large corrections that overshoot the fine-grid signature. These regions also show high sensitivity to grid refinement, indicating that a strong nonlinear process is present (e.g., shocks). These large overshoots are in locations where shock positions are changing with grid refinement. For example, the section of the signature  $X = [71 - 73]$  in Fig. 11(b) shows a strong sensitivity to grid refinement. Shock locations have the largest correction overshoot indicating locations with strong solution nonlinearities. The ETE correction appears to steepen expansions and sharpen pressure extrema. The large positive correction at  $X = 71$  without a negative correction upstream is in a location where the shock moves upstream with increasing grid refinement, Fig. 11(c). Banks et al.<sup>45</sup> showed that the correction computed with linearized ETE at discontinuities can grow locally unbounded with grid refinement. This observation indicates that nonlinear ETE should also be investigated for this class of problems, but the correction on the  $h = 1.00$  grid is smaller than  $h = 1.28$  grid for this case in Fig. 11(c).

The ETE solution on the symmetry plane of the  $h = 1.00$  grid is shown in Fig. 12. The correction is relatively small for the forward portion of the lower symmetry plane and larger for areas influenced by the tail. The lower extent of Fig. 12(a) is the one body length extraction location of Fig. 11. The locations of large correction seen in Fig. 11(b) correspond to the large values of correction that intercept the lower extent of Fig. 12(a), e.g., the large positive correction at  $X = 71$ . The correction in the extracted near-field can be tracked upstream to the source of the correction in Fig. 12. A closer examination of the symmetry plane around the tail of the configuration is shown in Fig. 12(b). The interior of the flow through nacelle has a

large correction. Large corrections radiate upward and downward from the tail structures. The parabolic correction feature aft of  $X = 35$  in Fig. 12(b) could be the intersection of the symmetry plane with a conic disturbance generated at the wing tip or horizontal tail tip.

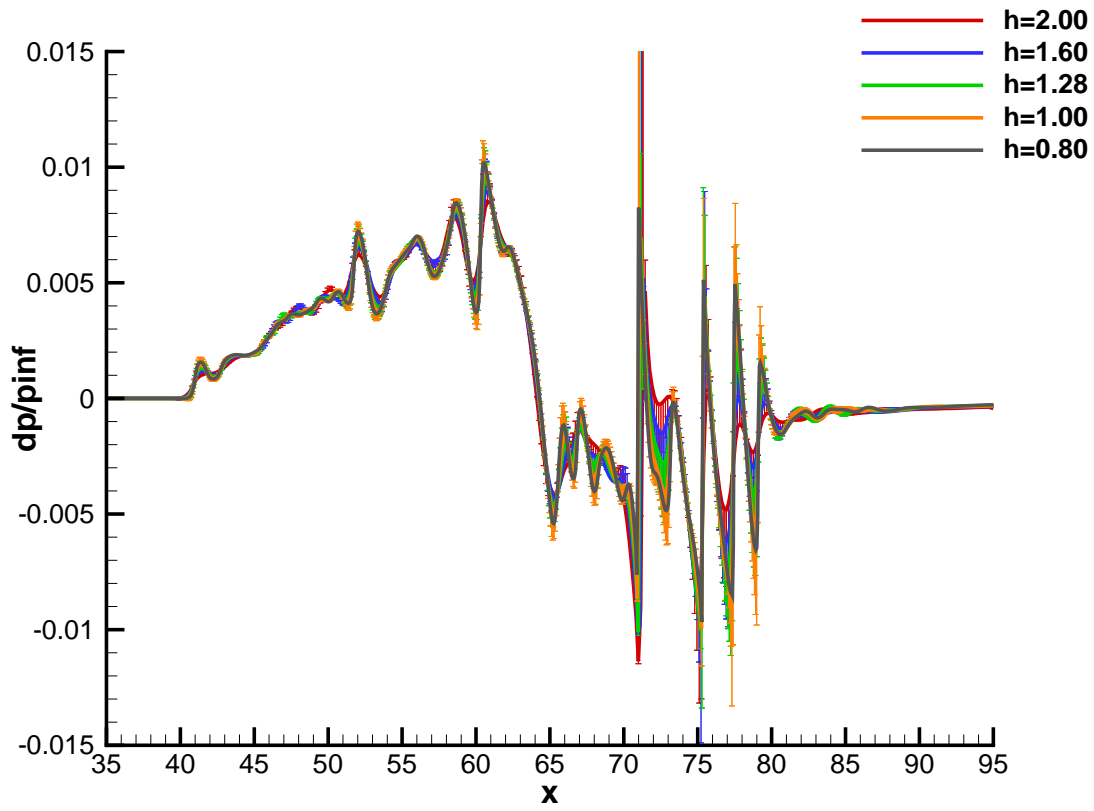
The error correction on the lower aft surface of the model is shown in Fig. 13. A low correction magnitude is generated by the wing with the exception of the wingtip. The lower portion of the fuselage under the wing has alternating areas of correction due to the triangular discretization of this area with compound curvature, but the correction does not propagate far from this location. The nacelle is surrounded by large corrections, which appear to ricochet between the wing and horizontal tail in Fig. 13. Regions of large correction are seen propagated downward from the trailing edges of the wing, fuselage, nacelle, horizontal tail, vertical tail, and vertical tail tip tank.

A view of the upper surface of the aft portion of the configuration is shown in Fig. 14. Blockage due to a pocket of subsonic air between the nacelle and the fuselage initiates a large correction that reflects inside of the flow through nacelle in Fig. 12(b). This correction also reflects off of the upper surface of the fuselage and wing. This same region of correction is reflected a second time by the horizontal tail and impacts the near-field signature at  $X = 71$  in Fig. 11. Some of the correction reflected by the upper surface of the wing continues around the leading edge of the horizontal tail to interact with the vertical tail tip tank, which radiates the correction in all directions. Foot prints of vortical structures near the leading edge of the wing, wing leading edge break, and horizontal tail are visible.

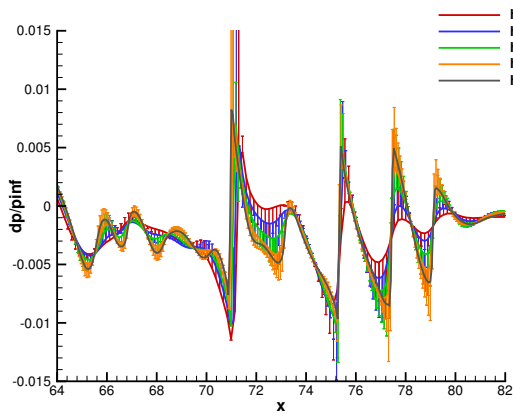
The ground signature propagated with sBOOM from near-field pressure at one body length is shown in Fig. 15. The ETE coupling is performed by extracting the complex-valued pressure from the FUN3D solution and providing it to a complex-valued version of sBOOM. The propagation is performed with an assumption of U.S. Standard Atmosphere<sup>53</sup> and humidity profile.<sup>54</sup> The ground has a reflection factor of 1.9. There are no winds and the aircraft is at 15,760m altitude. The smaller corrections in the forward portion of the near-field signature (Fig. 11) result in a smaller correction on the ground (Fig. 15). The regions of large correction in the aft portion of the near-field signature in Fig. 11(b) appear on the ground in Fig. 15(c). The correction predicts discretization error trends (due to grid refinement) in the forward portion of the signature, see Fig. 15(b), while strongly nonlinear propagation effects and large sensitivity to grid refinement are present in the aft portion of the signature, see Fig. 15(c). The shock at 0.112 seconds in the three coarsest grids is not present in the finest two grids. The direction of the error correction changes between the coarsest two grids and the next two finer grids, which could be a result of the inflection that is only present in the finer grid ground signatures. The  $h = 1.28$  grid shows the correction trends to the finer grids, but its real-valued signature is similar to the coarser two grids.

The loudness measure ASEL for the entire boom carpet is shown in Fig. 16 for three different extraction locations. The off track angle  $\phi$  is measured from a ray pointing from the aircraft to its ground track. The ASEL of the ground signatures shown in Fig. 15 is the  $\phi = 0$  of Fig. 16(a). The change in ground signature shape and correction for grids coarser and finer than the  $h = 1.28$  grid is seen in the ASEL and ASEL correction differences for  $\phi \leq 20$ . The sensitivity to grid refinement and correction sign are consistent for  $\phi \geq 30$ .

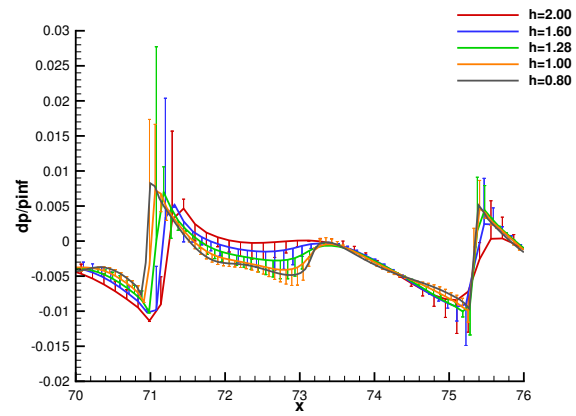
The strongly nonlinear ASEL calculation procedure shows differences between grid refinement and ETE, particularly where the CFD solution is under resolved. In regions of this strongly hyperbolic multidisciplinary analysis where the governing equations are sufficiently resolved, the  $h^\#$  ETE correction predicts both the trends and magnitude of the discretization error. The large ETE correction initiated near the inlet of the configuration can be tracked to correction values on the aircraft surface, symmetry plane, near-field pressure signature, ground signature, and ASEL noise measure through visual examination of the ETE solution.



(a) Full signature.

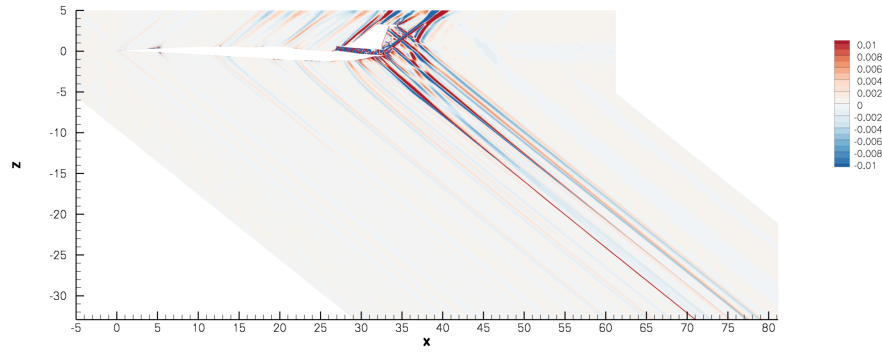


(b) Aft portion.

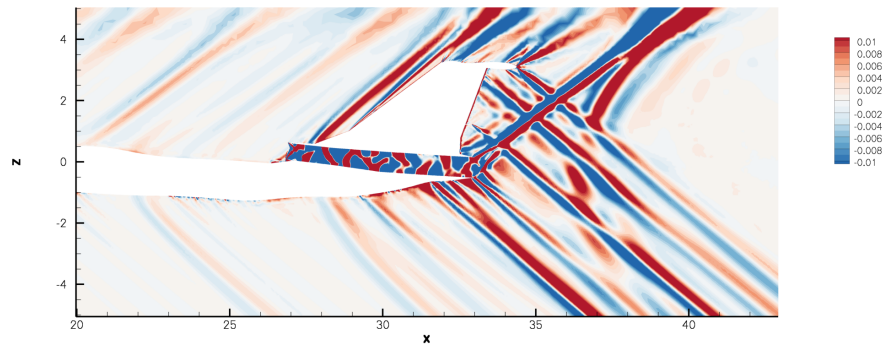


(c) Shock detail.

Figure 11. C25D nearfield pressure with correction at  $R/L = 1$ ,  $\phi = 0$ ,  $Z = -32.92$ .



(a) Extraction location at  $Z = -32.92$ .



(b) Zoom.

**Figure 12.** ETE of  $\Delta p/p_\infty$  on the symmetry plane of the C25D,  $h = 1.00$  grid.

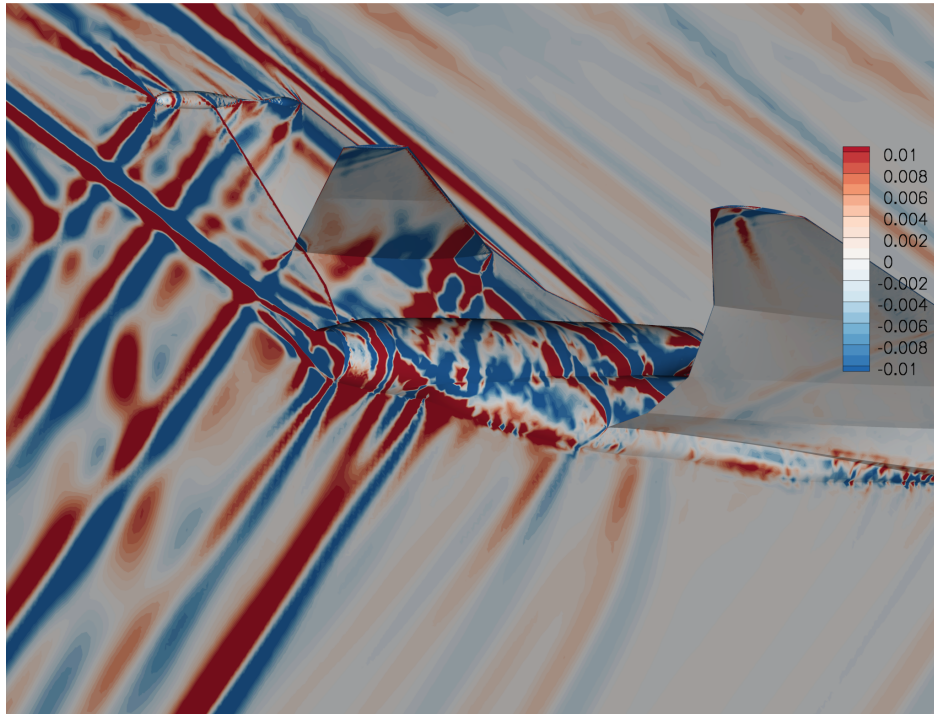


**Figure 13.** ETE of  $\Delta p/p_\infty$  on lower surface of the C25D,  $h = 1.00$  grid.

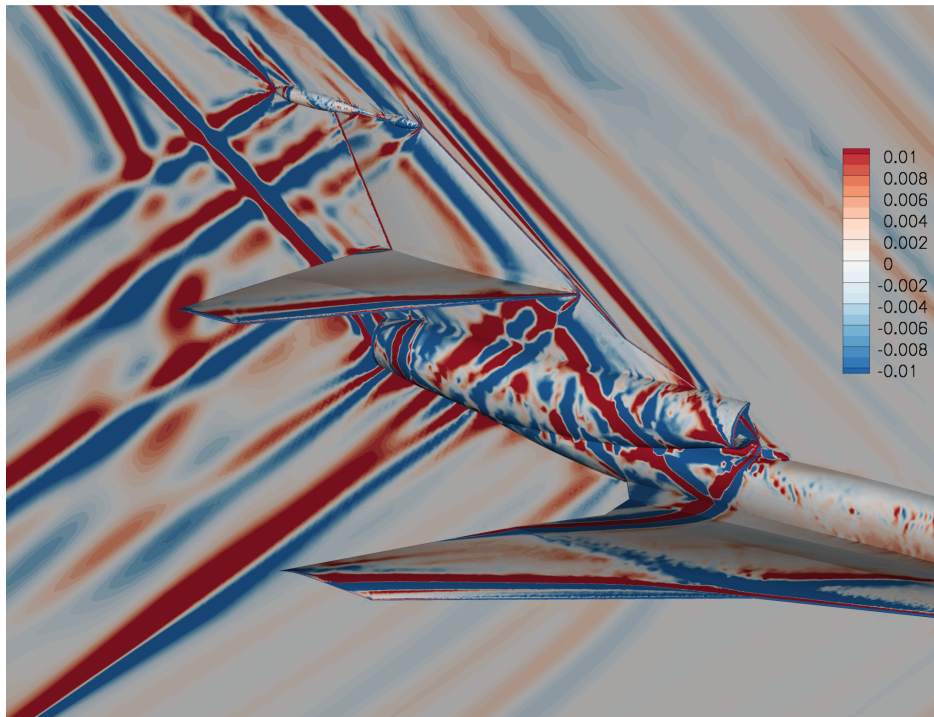
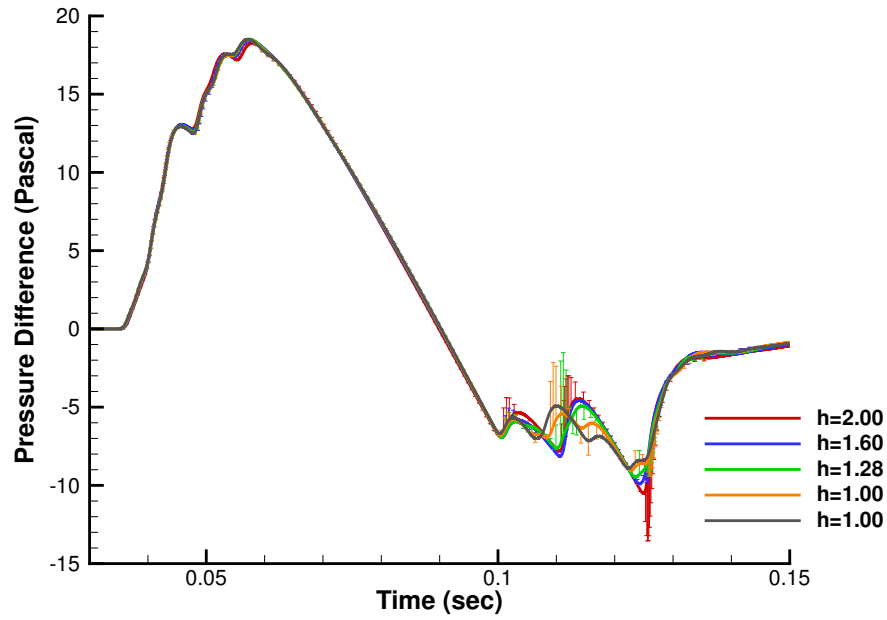
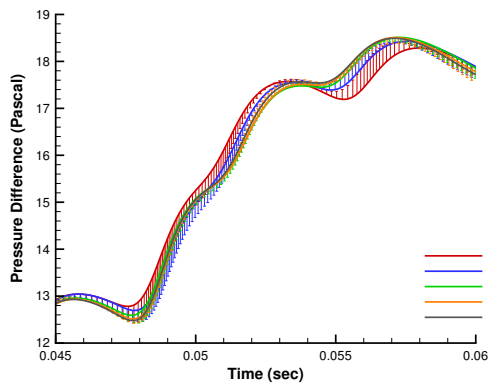


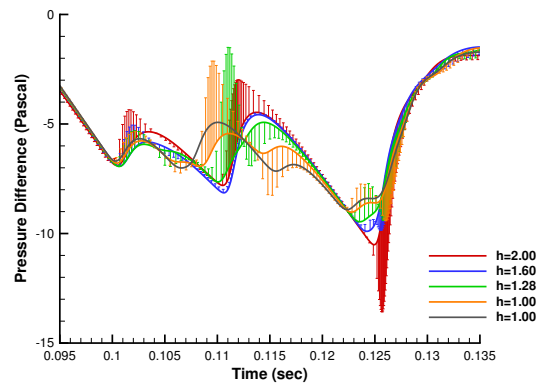
Figure 14. ETE of  $\Delta p/p_\infty$  on the upper surface of the C25D,  $h = 1.00$  grid.



(a) Full signature.



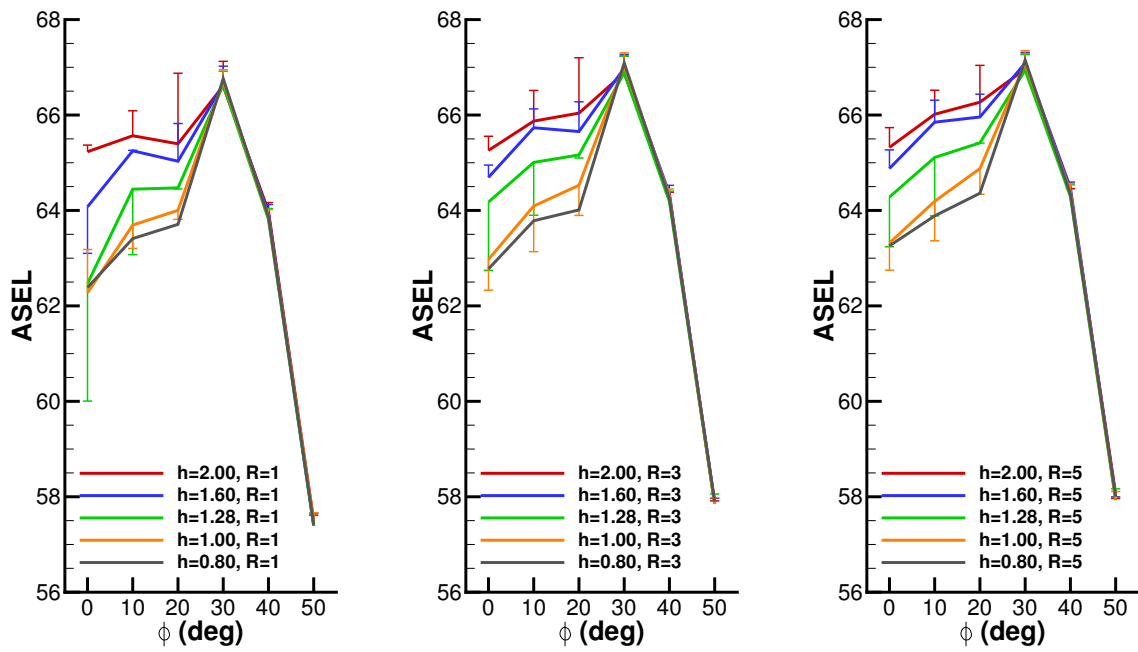
(b) Forward portion.



(c) Aft portion.

Figure 15. C25D ground with propagated correction from 1 body length on centerline.





(a) Pressure extracted at 1 body length. (b) Pressure extracted at 3 body length. (c) Pressure extracted at 5 body length.

Figure 16. C25D ASEL boom carpet with ETE from various extraction locations.

## VII. Conclusions

The equivalence of the adjoint functional error estimate and functional error estimates obtained by the ETE has been made. The ETE has several advantages compared to the adjoint method. It can provide an error estimate for any functional at the cost of a single solution as compared to the adjoint method, which requires one solution per functional. In addition, the ETE allows for visualization of local error estimates, allowing decision makers to better judge the accuracy of a computed solution. Detailed information about the generation and propagation of estimated discretization error can be obtained and connected to physical processes in a CFD or multi-discipline simulation. Without a good estimate of the truncation error (or residual error for  $h^\#$  error estimates) and a well-resolved flow field, both the ETE and adjoint methods may produce misleading error estimates. The ETE implementation uses a complex step approach to obtain exact linear sensitivities. The construction of the required complex-valued analysis codes is automated, includes the full capabilities of FUN3D, and permits the coupling of disciplines such as sBOOM atmospheric propagation and ASEL noise measure.

The use of the ETE has currently been applied to three AIAA prediction workshop cases to demonstrate the broad application of this ETE implementation. The limits on the utility of this linear method are shown for a range of problems, where the estimated errors approach finer grid solutions in an  $h^\#$  manner in some cases, or under- or over-estimate discretization error in regions with under-resolved flow features or strong nonlinearities. Output-based and norm-oriented grid adaptation provide tools to address the impact of these under resolved flow features by targeting remaining error estimates after the linear correction is applied. Developing complimentary ETE and adjoint error estimation methods is critical, because the ETE solution alone does not provide direct guidance to grid adaptation procedures. Further development of both  $h^\#$  and  $p^\#$  error estimates is critical to the success of both ETE and adjoint error estimation procedures. A system that combines adjoint-based adaptation and ETE has the potential to realize elements of CFD Vision 2030 by estimating, understanding the impact of, and reducing discretization error. Better methods for handling discretization error also support the understanding and management of other error sources. Ultimately, the combination of these tools will provide the guidance required to rigorously inform the risk management process at the program level.

## Acknowledgments

The authors would like to thank Carl Ollivier-Gooch (University of British Columbia) for helpful suggestions, as well as Steve Bauer, Pieter Buning, Bil Kleb (NASA Langley), Will Tyson (Virginia Tech), for reviews during the preparation of this manuscript. Kyle Thompson (NASA Langley) implemented complex-valued restarts from a real-valued solution in FUN3D. The authors would like to thank the Revolutionary Vertical Lift Technology (RVLT) Project and the Commercial Supersonic Transport (CST) Project of the Advanced Air Vehicles Program and the Transformational Tools and Technologies (TTT) Project of the Transformative Aeronautics Concepts Program (TACP) for supporting this work.

## References

- <sup>1</sup>Slotnick, J., Khodadoust, A., Alonso, J., Darmofal, D., Gropp, W., Lurie, E., and Mavriplis, D., “CFD Vision 2030 Study: A Path to Revolutionary Computational Aerosciences,” NASA CR-2014-218178, March 2014. doi:2060/20140003093.
- <sup>2</sup>Walker, E. L., Hemsch, M. J., and West, IV, T. K., “Integrated Uncertainty Quantification for Risk and Resource Management: Building Confidence in Design,” AIAA Paper 2015-501, 2015.
- <sup>3</sup>Lee, H. B., Ghia, U., Bayyuk, S., Oberkampf, W., Roy, C. J., Benek, J., Rumsey, C. L., Powers, J., Bush, R. H., and Mani, M., “Development and Use of Engineering Standards for Computational Fluid Dynamics for Complex Aerospace Systems,” AIAA Paper 2016-3811, 2016.
- <sup>4</sup>Oberkampf, W. L. and Roy, C. J., *Verification and Validation in Scientific Computing*, Cambridge University Press, 2010.
- <sup>5</sup>Mavriplis, D. J., Vassberg, J. C., Tinoco, E. N., Mani, M., Brodersen, O. P., Eisfeld, B., Wahls, R. A., Morrison, J. H., Zickuhr, T., Levy, D., and Murayama, M., “Grid Quality and Resolution Issues from the Drag Prediction Workshop Series,” *AIAA Journal of Aircraft*, Vol. 46, No. 3, 2009, pp. 935–950. doi:10.2514/1.39201.
- <sup>6</sup>Pelletier, D., Zaki, A., and Fortin, A., “Adaptive Remeshing for Hyperbolic Transport Problems,” *International Journal of Computational Fluid Dynamics*, Vol. 3, No. 2, 1994, pp. 79–99. doi:10.1080/10618569408904501.
- <sup>7</sup>Biedron, R. T., Carlson, J.-R., Derlaga, J. M., Gnoffo, P. A., Hammond, D. P., Jones, W. T., Kleb, B., Lee-Rausch, E. M., Nielsen, E. J., Park, M. A., Rumsey, C. L., Thomas, J. L., and Wood, W. A., “FUN3D Manual: 13.0,” NASA TM-2016-219330, Langley Research Center, Aug. 2016. doi:2060/20160010563.

- <sup>8</sup>Fidkowski, K. J. and Darmofal, D. L., "Review of Output-Based Error Estimation and Mesh Adaptation in Computational Fluid Dynamics," *AIAA Journal*, Vol. 49, No. 4, 2011, pp. 673–694. doi:10.2514/1.J050073.
- <sup>9</sup>Anderson, W. K., Newman, J. C., Whitfield, D. L., and Nielsen, E. J., "Sensitivity Analysis for the Navier-Stokes Equations on Unstructured Meshes Using Complex Variables," *AIAA Journal*, Vol. 39, No. 1, 2001, pp. 56–63. doi:10.2514/2.1270.
- <sup>10</sup>Levy, D. W., Laffin, K. R., Tinoco, E. N., Vassberg, J. C., Mani, M., Rider, B., Rumsey, C. L., Wahls, R. A., Morrison, J. H., Brodersen, O. P., Crippa, S., Mavriplis, D. J., and Murayama, M., "Summary of Data from the Fifth Computational Fluid Dynamics Drag Prediction Workshop," *AIAA Journal of Aircraft*, Vol. 51, No. 4, 2014, pp. 1194–1213. doi:10.2514/1.C032389.
- <sup>11</sup>Rumsey, C. L. and Slotnick, J. P., "Overview and Summary of the Second AIAA High Lift Prediction Workshop," *AIAA Journal of Aircraft*, Vol. 52, No. 4, 2015, pp. 1006–1025. doi:10.2514/1.C032864.
- <sup>12</sup>Park, M. A. and Morgenstern, J. M., "Summary and Statistical Analysis of the First AIAA Sonic Boom Prediction Workshop," *AIAA Journal of Aircraft*, Vol. 51, No. 2, 2016, pp. 578–598. doi:10.2514/1.C033449.
- <sup>13</sup>Cavallo, P. A. and Sinha, N., "Error Quantification for Computational Aerodynamics Using an Error Transport Equation," *AIAA Journal of Aircraft*, Vol. 44, No. 6, 2007. doi:10.2514/1.33154.
- <sup>14</sup>Cavallo, P. A., O’Gara, M. R., Feldman, G. M., and Liu, Z., "Unified Error Transport Equation Solver for Solution Verification on Unstructured Grids," AIAA Paper 2012–3345, 2012.
- <sup>15</sup>Cavallo, P. A., "CRUNCH CFD Calculations for HiLiftPW-2 with Discretization Error Predictions," AIAA Paper 2014–916, 2014.
- <sup>16</sup>Phillips, T. S., *Residual-based Discretization Error Estimation for Computational Fluid Dynamics*, Ph.D. thesis, Virginia Polytechnic Institute and State University, Sept. 2014. doi:10919/50647.
- <sup>17</sup>Derlaga, J. M., *Application of Improved Truncation Error Estimation Techniques to Adjoint Based Error Estimation and Grid Adaptation*, Ph.D. thesis, Virginia Polytechnic Institute and State University, July 2015. doi:10919/54592.
- <sup>18</sup>Tyson, W. C., Swirydowicz, K., Derlaga, J. M., Roy, C. J., and de Sturler, E., "Improved Functional-Based Error Estimation and Adaptation without Adjoints," AIAA Paper 2016–3809, 2016.
- <sup>19</sup>Nielsen, E. J. and Kleb, W. L., "Efficient Construction of Discrete Adjoint Operators on Unstructured Grids Using Complex Variables," *AIAA Journal*, Vol. 44, No. 4, 2006, pp. 827–836. doi:10.2514/1.15830.
- <sup>20</sup>Martins, J. R. A., Sturdza, P., and Alonso, J. J., "The Complex-Step Derivative Approximation," *ACM Transactions on Mathematical Software (TOMS)*, Vol. 29, No. 3, 2003, pp. 245–262. doi:10.1145/838250.838251.
- <sup>21</sup>Nielsen, E. J., *Aerodynamic Design Sensitivities on an Unstructured Mesh Using the Navier-Stokes Equations and a Discrete Adjoint Formulation*, Ph.D. thesis, Virginia Polytechnic Institute and State University, 1998.
- <sup>22</sup>Lee-Rausch, E. M., Park, M. A., Jones, W. T., Hammond, D. P., and Nielsen, E. J., "Application of a Parallel Adjoint-Based Error Estimation and Anisotropic Grid Adaptation for Three-Dimensional Aerospace Configurations," AIAA Paper 2005–4842, 2005.
- <sup>23</sup>Pierce, N. A. and Giles, M. B., "Adjoint Recovery of Superconvergent Functionals from PDE Approximations," *SIAM Review*, Vol. 42, No. 2, 2000, pp. 247–264.
- <sup>24</sup>Yan, G. K. K. and Ollivier-Gooch, C. F., "Accuracy of Discretization Error Estimation by the Error Transport Equation on Unstructured Meshes," AIAA Paper 2015–1264, 2015.
- <sup>25</sup>Venditti, D. A. and Darmofal, D. L., "Grid Adaptation for Functional Outputs: Application to Two-Dimensional Inviscid Flows," *Journal of Computational Physics*, Vol. 176, No. 1, 2002, pp. 40–69. doi:10.1006/jcph.2001.6967.
- <sup>26</sup>Venditti, D. A. and Darmofal, D. L., "Anisotropic Grid Adaptation for Functional Outputs: Application to Two-Dimensional Viscous Flows," *Journal of Computational Physics*, Vol. 187, No. 1, 2003, pp. 22–46. doi:10.1016/S0021-9991(03)00074-3.
- <sup>27</sup>Venditti, D. A., *Grid Adaptation for Functional Outputs of Compressible Flow Simulations*, Ph.D. thesis, Massachusetts Institute of Technology, June 2002. doi:1721.1/29246.
- <sup>28</sup>Park, M. A., "Adjoint-Based, Three-Dimensional Error Prediction and Grid Adaptation," *AIAA Journal*, Vol. 42, No. 9, 2004, pp. 1854–1862. doi:10.2514/1.10051.
- <sup>29</sup>Park, M. A., "Three-Dimensional Turbulent RANS Adjoint-Based Error Correction," AIAA Paper 2003–3849, 2003.
- <sup>30</sup>Anderson, W. K. and Bonhaus, D. L., "An Implicit Upwind Algorithm for Computing Turbulent Flows on Unstructured Grids," *Computers and Fluids*, Vol. 23, No. 1, 1994, pp. 1–22. doi:10.1016/0045-7930(94)90023-X.
- <sup>31</sup>Anderson, W. K. and Venkatakrishnan, V., "Aerodynamic Design Optimization on Unstructured Grids with a Continuous Adjoint Formulation," *Computers and Fluids*, Vol. 28, No. 4–5, 1999, pp. 443–480. doi:10.1016/S0045-7930(98)00041-3.
- <sup>32</sup>Pierce, N. and Giles, M., "Adjoint and Defect Error Bounding and Correction for Functional Estimates," *Journal of Computational Physics*, Vol. 200, No. 2, 2004, pp. 769–794. doi:10.1016/j.jcp.2004.05.001.
- <sup>33</sup>Plotkin, K. J., "State of the Art of Sonic Boom Modeling," *Journal of the Acoustical Society of America*, Vol. 111, No. 1, 2002, pp. 530–536. doi:10.1121/1.1379075.
- <sup>34</sup>Rallabhandi, S. K., "Advanced Sonic Boom Prediction Using the Augmented Burgers Equation," *AIAA Journal of Aircraft*, Vol. 48, No. 4, 2011, pp. 1245–1253. doi:10.2514/1.C031248.
- <sup>35</sup>Shepherd, K. P. and Sullivan, B. M., "A Loudness Calculation Procedure Applied to Shaped Sonic Booms," NASA TP-3134, Nov. 1991. doi:2060/19920002547.
- <sup>36</sup>Rallabhandi, S. K., Nielsen, E. J., and Diskin, B., "Sonic Boom Mitigation Through Aircraft Design and Adjoint Methodology," *AIAA Journal of Aircraft*, Vol. 51, No. 2, 2014. doi:10.2514/1.C032189.
- <sup>37</sup>Loubeau, A., Naka, Y., Cook, B. G., Sparrow, V. W., and Morgenstern, J. M., "A New Evaluation of Noise Metrics for Sonic Booms Using Existing Data," *2nd International Sonic Boom Forum*, 20th International Symposium on Nonlinear Acoustics, July 2015.
- <sup>38</sup>Rimell, A. N., Mansfield, N. J., and Paddan, G. S., "Design of Digital Filters for Frequency Weightings (A and C) Required for Risk Assessments of Workers Exposed to Noise," *Industrial Health*, Vol. 53, No. 1, 2015, pp. 21–27. doi:10.2486/indhealth.2013-0003.

- <sup>39</sup>Silva, W. A., Sanetrik, M. D., Chwalowski, P., Connolly, J., and Kopasakis, G., “Using FUN3D for Aeroelastic, Sonic Boom, and AeroPropulsoServoElastic (APSE) Analyses of a Supersonic Configuration,” AIAA Paper 2016–1319, 2016.
- <sup>40</sup>Connolly, J. W., Kopasakis, G., Chwalowski, P., Sanetrik, M. D., Carlson, J.-R., Silva, W. A., and McNamara, J., “Towards an Aero-Propulso-Servo-Elasticity Analysis of a Commercial Supersonic Transport,” AIAA Paper 2016–1320, 2016.
- <sup>41</sup>Mishra, A., Mani, K., Mavriplis, D., and Sitaraman, J., “Time Dependent Adjoint-Based Optimization for Coupled Fluid–Structure Problems,” *Journal of Computational Physics*, Vol. 292, 2015, pp. 253–271. doi:10.1016/j.jcp.2015.03.010.
- <sup>42</sup>Park, M. A., *Anisotropic Output-Based Adaptation with Tetrahedral Cut Cells for Compressible Flows*, Ph.D. thesis, Massachusetts Institute of Technology, Sept. 2008. doi:1721.1/46363.
- <sup>43</sup>Park, M. A., Krakos, J. A., Michal, T., Loseille, A., and Alonso, J. J., “Unstructured Grid Adaptation: Status, Potential Impacts, and Recommended Investments Toward CFD Vision 2030,” AIAA Paper 2016–3323, 2016.
- <sup>44</sup>Loseille, A., Dervieux, A., and Alauzet, F., “Anisotropic Norm-Oriented Mesh Adaptation for Compressible Inviscid Flows,” AIAA Paper 2015–2037, 2015.
- <sup>45</sup>Banks, J. W., Hittinger, J. A. F., Connors, J. M., and Woodward, C. S., “Numerical Error Estimation for Nonlinear Hyperbolic PDEs via Nonlinear Error Transport,” *Computer Methods in Applied Mechanics and Engineering*, Vol. 213–216, 2012, pp. 1–15. doi:10.1016/j.cma.2011.11.021.
- <sup>46</sup>Cavallo, P. A., O’Gara, M. R., and Schikore, D. R., “Software System for Prediction, Visualization, Analysis, and Reduction of Errors in CFD Simulations,” AIAA Paper 2009–3349, 2009.
- <sup>47</sup>Rumsey, C. L., Slotnick, J. P., Long, M., Stuever, R. A., and Wayman, T. R., “Summary of the First AIAA CFD High-Lift Prediction Workshop,” *AIAA Journal of Aircraft*, Vol. 48, No. 6, 2011, pp. 2068–2079. doi:10.2514/1.C031447.
- <sup>48</sup>Wintzer, M., Ordaz, I., and Fenbert, J. W., “Under-Track CFD-Based Shape Optimization for a Low-Boom Demonstrator Concept,” AIAA Paper 2015–2260, 2015.
- <sup>49</sup>Ordaz, I., Wintzer, M., and Rallabhandi, S. K., “Full-Carpet Design of a Low-Boom Demonstrator Concept,” AIAA Paper 2015–2261, 2015.
- <sup>50</sup>Wintzer, M., *Optimization and Adjoint-Based CFD for the Conceptual Design of Low Sonic Boom Aircraft*, Ph.D. thesis, Stanford University, Aug. 2012.
- <sup>51</sup>Dannenhoffer, III, J. F., “OpenCSM: An Open-Source Constructive Solid Modeler for MDAO,” AIAA Paper 2013–701, 2013.
- <sup>52</sup>Park, M. A., Campbell, R. L., Elmiligui, A., Cliff, S. E., and Nayani, S. N., “Specialized CFD Grid Generation Methods for Near-Field Sonic Boom Prediction,” AIAA Paper 2014–115, 2014.
- <sup>53</sup>*U.S. Standard Atmosphere, 1976*, U.S. Government Printing Office, 1976.
- <sup>54</sup>American National Standards Institute, “Method for Calculation of the Absorption of Sound by the Atmosphere,” ANSI S1.26-1995, Sept. 1995.